



# Fast correction approach for wavefront sensorless adaptive optics based on a linear phase diversity technique

DAN YUE,<sup>1,\*</sup> HAITAO NIE,<sup>2</sup> YE LI,<sup>1</sup> AND CHANGSHENG YING<sup>1</sup>

<sup>1</sup>College of Science, Changchun University of Science and Technology, Changchun 130022, China

<sup>2</sup>Changchun Institute of Optics, Fine Mechanics and Physics, Chinese Academy of Sciences, Changchun 130033, China

\*Corresponding author: danzik3@126.com

Received 27 November 2017; revised 26 January 2018; accepted 26 January 2018; posted 29 January 2018 (Doc. ID 314116); published 27 February 2018

Wavefront sensorless (WFSless) adaptive optics (AO) systems have been widely studied in recent years. To reach optimum results, such systems require an efficient correction method. This paper presents a fast wavefront correction approach for a WFSless AO system mainly based on the linear phase diversity (PD) technique. The fast closed-loop control algorithm is set up based on the linear relationship between the drive voltage of the deformable mirror (DM) and the far-field images of the system, which is obtained through the linear PD algorithm combined with the influence function of the DM. A large number of phase screens under different turbulence strengths are simulated to test the performance of the proposed method. The numerical simulation results show that the method has fast convergence rate and strong correction ability, a few correction times can achieve good correction results, and can effectively improve the imaging quality of the system while needing fewer measurements of CCD data. © 2018 Optical Society of America

**OCIS codes:** (110.1080) Active or adaptive optics; (220.1000) Aberration compensation; (110.0115) Imaging through turbulent media; (010.7350) Wave-front sensing.

<https://doi.org/10.1364/AO.57.001650>

## 1. INTRODUCTION

Conventional adaptive optics (AO) systems usually utilize a wavefront sensor to detect the distorted wavefront phase information and a wavefront corrector such as a deformable mirror (DM) to correct the incoming aberrated wavefront [1,2]. The Shack–Hartmann wavefront sensor is widely used in conventional AO systems due to its fast speed and high precision. However, with the extension of AO application fields, such as free-space optical communication, extended target imaging, laser cavity aberration correction, and non-coherent beam imaging [3,4], the ability of conventional adaptive optics is gradually limited; wavefront sensorless (WFSless) AO technology has become a research hotspot.

The WFSless AO system directly takes the control signal required by the wavefront corrector as the optimization parameters and the system performance index, such as imaging clarity or receiving light energy, as the objective function of the control algorithm, and then obtains the ideal correction results by optimization methods. For now, the WFSless AO system can be divided into non-model algorithm systems or model-based algorithm systems according to different optimization methods. The non-model-based system takes the various blind

optimization algorithms, such as the stochastic parallel gradient descent algorithm [5,6], simulated annealing [7], genetic algorithm [8], and hill-climbing algorithm [9], as the system control algorithm in contrast to the model-based system. The slow convergence speed is the largest defect of the non-model AO system. The model-based WFSless AO system first establishes a system model based on certain principles, such as the model method [10,11], the non-linear optimization method [12], or the geometrical optics principle [13], then determines to take the corresponding system control algorithm. It has a relatively fast convergence rate, but needs to define different types of basis functions or establish the non-linear equation model for input and output of the system and clear out the system aberration before correction.

In order to reach optimum results for the WFSless AO system, an efficient correction method is needed. This paper presents a fast wavefront correction method for the WFSless AO system based on the linear phase diversity (PD) technique. It mainly focuses on establishing the linear analytic model between the far-field distortion images obtained by CCD cameras and the drive voltage of the DM to realize the fast wavefront correction. The paper is organized as follows. In Section 2, we

give the structure of the WFSless AO system and briefly introduce the working principle of the method. The detailed closed-loop control algorithm and correction process are presented in Section 3. A large number of simulations are performed in Section 4 to verify the convergence speed and the correction ability of the proposed method. In the last section, we summarize our work and give the conclusion.

## 2. SYSTEM STRUCTURE AND WORKING PRINCIPLE

The structure of the WFSless AO system based on the linear PD technique is shown in Fig. 1. It consists of a host control computer, a DM, an imaging system, a linear PD algorithm module, and a wavefront corrector drive control circuit module. Since the PD algorithm needs a pair of simultaneously collected images to reconstruct the wavefront [14,15], it is necessary to add an extra camera to the imaging system to acquire the other out-of-focus image. Therefore, the imaging system is composed of a beam splitter prism, two imaging lenses, and two CCD cameras, which are used to collect the distorted images in the focal plane and out-of-focal plane, respectively.

When it works, the wavefront to be corrected is reflected to the beam splitter prism by the DM, and the beam splitter prism divides it into two beams, and then the imaging lens focuses them into their respective CCD cameras. The images in the focal plane and out-of-focal plane obtained by the CCD cameras are collected to the host control computer by the image acquisition card in high speed. Based on the linear PD algorithm and combined with the influence function of the DM, the linear relationship model of the far-field images and drive voltage of the wavefront corrector is established in advance. Then the corresponding drive control voltage is directly computed according to the established linear relationship model and output the control computer. The drive circuit applies the output voltage to the DM to generate the compensation amount for the aberrated wavefront, then the fast wavefront correction is realized and the ideal imaging effect can be obtained in the end.

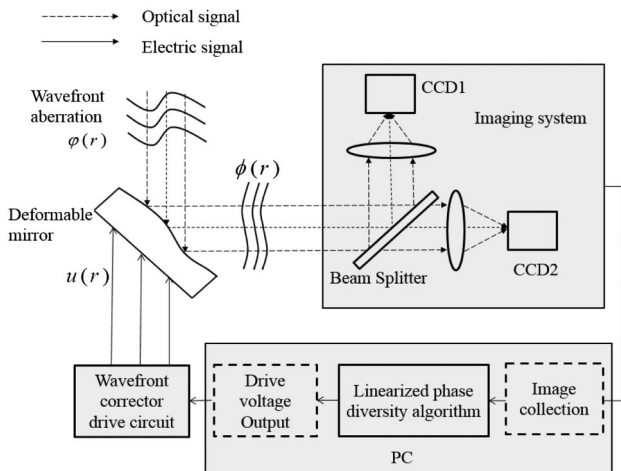


Fig. 1. Block diagram of WFSless AO system based on linear PD technique.

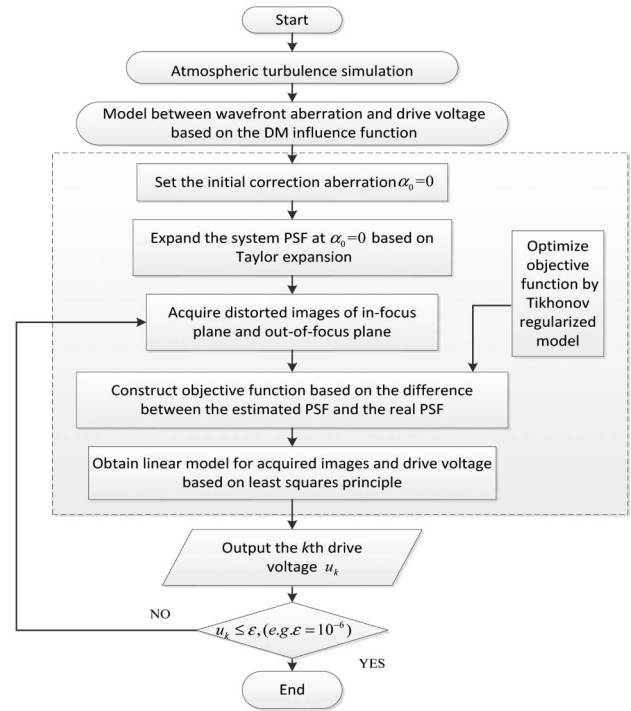


Fig. 2. Overall flow chart of the closed-loop control algorithm.

## 3. CLOSED-LOOP CONTROL ALGORITHM

When the incident beam is not ideal, the image acquired by the imaging system is distorted, which contains the wavefront aberration information. The PD algorithm is the kind of technology that utilizes the far-field images to reconstruct the wavefront. In our work, a fast closed-loop algorithm is proposed based on the linear PD technology and combined with the influence function of the DM. The overall closed-loop control flow chart is shown in Fig. 2, which mainly includes the DM module and linear PD algorithm module. The DM module is about establishing the linear relationship between the wavefront aberration and the drive voltage of the wavefront corrector, and the linear PD algorithm module focuses on constructing the linear analytic model between the far-field images and the drive voltage based on the DM module. The following part will give a detailed description for the proposed closed-loop control algorithm mainly based on these two modules.

### A. DM Module

According to the working principle of the wavefront corrector, the shape change of the DM can be expressed by the linear combination of each actuator's influence function, shown in Eq. (1):

$$\Delta\phi(r) = \sum_i^N u_i S_i(r), \quad (1)$$

where  $S_i(r)$  is the influence function of the  $i$ th actuator,  $u_i$  is the drive voltage applied to the  $i$ th actuator,  $\Delta\phi(r)$  denotes the deformation amount of the mirror, and  $N$  is the number of actuators. In our simulation, a 140-element DM is used and

the influence function of each actuator of the DM can be measured by a ZYGO interferometer.

Meanwhile, the wavefront can be fitted by Zernike polynomials, so the shape change of the DM can also be expressed as Eq. (2):

$$\Delta\phi(r) = \sum_j^M \alpha_j Z_j(r), \quad (2)$$

where  $M$  is the number of the Zernike order, and  $\alpha_j$  is the  $j$ th order Zernike coefficient.

In order to establish the relationship between the influence function of the DM and the Zernike polynomial, each actuator's influence function can be written in the form of Zernike polynomials, shown as Eq. (3):

$$S_i(r) = \sum_j^M \alpha_{ij} Z_j(r), \quad (3)$$

where  $\alpha_{ij}$  is the  $j$ th order Zernike coefficient of the  $i$ th actuator's influence function.

Combining Eq. (1) with Eq. (3) and taking the result into Eq. (2), we get the following equation:

$$\sum_j^M \alpha_j Z_j(r) = \sum_i^N \sum_j^M u_i \alpha_{ij} Z_j(r). \quad (4)$$

Getting rid of  $Z_j(r)$  on both sides of Eq. (4) and writing the result in matrix form, we get Eq. (5):

$$\alpha = \mathbf{C}_{zv} \bullet \mathbf{u}, \quad (5)$$

where  $\mathbf{C}_{zv}$  denotes the correlation matrix between the influence function and Zernike coefficients,  $\mathbf{u}$  represents the drive voltage matrix of the DM,  $\alpha$  represents the Zernike aberration coefficient matrix, and  $\bullet$  represents a matrix multiplication; see [16,17].

Thus, the linear relationship model of the drive voltage of the DM and wavefront aberration coefficients can be established directly, shown as Eq. (6):

$$\mathbf{u} = \mathbf{C}_{zv}^\dagger \bullet \alpha, \quad (6)$$

where  $\dagger$  stands for the pseudoinverse of the matrix. It can be seen from Eq. (6) that the variables to be solved have been transferred from the Zernike coefficients directly to the DM driver control voltage. As the DM is determined, the above matrices are prior known quantities and can be saved as known matrices to be used directly during the wavefront corrections in the later.

## B. Linearized PD Algorithm Module

The PD technique uses the images in the focal and the out-of-focal planes to calculate the wavefront aberrations. Based on the Fourier optical imaging principle, the images in the focal and the out-of-focal planes can be gained by Eq. (7):

$$\begin{aligned} i_f(u, v) &= o * p_s f_f(u, v) + n(u, v), \\ i_d(u, v) &= o * p_s f_d(u, v) + n(u, v), \end{aligned} \quad (7)$$

where  $i_f$  and  $i_d$  are the images in the focal and the out-of-focal planes, respectively;  $o$  stands for the observation target;  $p_s f_f$  and  $p_s f_d$  represent point spread function (PSF) of the focal

and the out-of-focal channels, respectively;  $n(u, v)$  is the noise term of the CCD camera; and  $*$  represents convolution operation. The image obtained on the far-field imaging plane can be simplified as the PSF of the system when the observation target is the non-extended target, such as the point source.

According to the Fourier optics principle, the relationship between the system PSF and the incident wavefront phase can be expressed by Eq. (8):

$$p_s f(u, v) = |\mathfrak{F}[A \exp(i\phi(r))]|^2, \quad (8)$$

where  $\mathfrak{F}$  stands for the Fourier transform operation,  $A$  represents the pupil shape function,  $\phi(r)$  is the phase of the incident beam which is fitted by Zernike polynomials  $\phi(r) = \sum_i^M \alpha_i Z_i(r)$ , and  $\alpha$  stands for the Zernike coefficients.

The system PSF can be linearly approximated based on the first-order Taylor expansion at 0 aberration, shown in Eq. (9):

$$p_s f(\alpha) = h_0 + h_1 \cdot \alpha + O\|\alpha\|^2, \quad (9)$$

where  $h_0 = p_s f(\alpha)|_{\alpha=0}$ ,  $h_1 = \frac{\partial p_s f}{\partial \alpha}|_{\alpha=0}$ , and  $O\|\alpha\|^2$  is the second-order Lagrange residue. When the phase is very small, the second-order residue can be ignored.

Based on the least-squares principle, a cost function can be constructed utilizing the difference between the actual spot images obtained by the CCD cameras and that we rebuilt by linear approximation; the smaller the difference is, the more accurate the rebuilt wavefront aberration is [15]. In order to suppress the influence of CCD camera noise on the accuracy of wavefront reconstruction, we introduce a Tikhonov regularization model to optimize the cost function at the same time. Then the final constructed cost function is given in Eq. (10):

$$E = \|p_s f_f(\alpha) - i_f\|_2^2 + \|p_s f_d(\alpha) - i_d\|_2^2 + \lambda \|L_i \alpha\|_2^2, \quad (10)$$

where  $\lambda \|L_i \alpha\|_2^2$  is the introduced Tikhonov regularization parameter term,  $\lambda$  is the non-negative regularization parameter related with CCD noise, and  $L_i$  is the  $i$ th differential operator.

Taking the linearized PSFs of the focal and out-of-focal planes to Eq. (10) and ignoring the second-order residue, we get

$$E = \|h_{1,f} \cdot \alpha + h_{0,f} - i_f\|_2^2 + \|h_{1,d} \cdot \alpha + h_{0,d} - i_d\|_2^2 + \lambda \|L_i \alpha\|_2^2, \quad (11)$$

where  $h_{0,f}$  and  $h_{1,f}$  are the  $h_0$  and  $h_1$  of the focal plane, and  $h_{0,d}$  and  $h_{1,d}$  are the  $h_0$  and  $h_1$  of the out-of-focal plane, respectively.

In order to find the minimum value of the cost function we make  $\partial E / \partial \alpha = 0$ ; the calculation result is shown in Eq. (12):

$$U_1^T U_1 \alpha - U_1^T W_1 + U_2^T U_2 \alpha - U_2^T W_2 + \lambda L_i^T L_i \alpha = 0, \quad (12)$$

among which,  $U_1 = h_{1,f}$ ,  $U_2 = h_{1,d}$ ,  $W_1 = i_f - h_{0,f}$ , and  $W_2 = i_d - h_{0,d}$ .

Using the least-square method to solve Eq. (12), the wavefront aberration of the system can be obtained:

$$\hat{\alpha} = [\Re(U_1^T U_1 + U_2^T U_2 + \lambda L_i^T L_i)]^\dagger [\Re(U_1^T W_1 + U_2^T W_2)], \quad (13)$$

where  $\Re$  represents the real part operator,  $\dagger$  is the generalized inverse of a matrix, and  $\bullet^T$  denotes the matrix transposition.

Simplifying Eq. (13) into matrix form, we get the linear relationship model between aberrations and acquired images in Eq. (14):

$$\hat{\alpha} = \mathbf{H} \cdot [\mathbf{i}_f^T, \mathbf{i}_d^T]. \quad (14)$$

Combined with Eq. (6), a direct linear relationship between the acquired images and the drive voltage of the DM can be established, as shown in Eq. (15):

$$\mathbf{u} = \mathbf{C}_{zv}^\dagger \cdot \mathbf{H} \cdot [\mathbf{i}_f^T, \mathbf{i}_d^T]. \quad (15)$$

Let  $\mathbf{D} = \mathbf{C}_{zv}^\dagger \cdot \mathbf{H}$ , the above formula can be finally written as

$$\mathbf{u} = \mathbf{D} \cdot [\mathbf{i}_f^T, \mathbf{i}_d^T], \quad (16)$$

where  $\mathbf{D}$  is our proposed image-voltage matrix. Thus, we can directly output the drive voltage of the DM by the input distorted far-field images of the system.

### C. Correction Process of the Control Algorithm

The correction process of the control algorithm can be divided into the preprocessing step and the iteration step. The preprocessing step includes two parts: calculating the correlation matrix between the influence function and Zernike coefficients  $\mathbf{C}_{zv}$  by fitting the influence function of each actuator using Zernike polynomials, and computing the PSFs of the focal plane and the out-of-focal plane and their corresponding first derivative values at  $\mathbf{0}$  aberration. Since all these values are independent of the system wavefront aberration to be corrected, they can be precalculated and saved as known matrices to be called directly during the subsequent calibrations.

Based on the preprocessing step, the iteration step is carried out as below. According to Eq. (16), the initial correction voltage  $\mathbf{u}_0$  can be obtained directly using the spot images captured in the focal plane and the out-of-focal plane for the first time. Then drive the DM to generate the compensation wavefront  $u_0(r)$ , and the corrected residual wavefront is  $\phi_1(r) = \phi_0(r) - u_0(r)$ , where  $\phi_0(r)$  stands for the original wavefront. Then, we acquire the spot images after correction again as the new pair of far-field images, and repeat the above steps to get a new correction voltage and drive the DM to correct the residual aberration repeatedly. Supposing that the  $k$ th correction voltage is  $\mathbf{u}_k$  and the corresponding compensation wavefront is  $u_k(r)$ , then the residual wavefront after  $k$ th correction is  $\phi_{k+1}(r) = \phi_k(r) - u_k(r)$ . When the calculated drive voltage approaches zero, the wavefront closed-loop correction process is finished.

The reason that our method takes a few iterations to correct the wavefront is that we ignore the second-order Lagrange residue in Eq. (9) in order to establish the linear model in Eq. (13), while the neglect is only allowed when the phase is small. This leads to the calculated  $u(r)$  having a relatively large deviation from the actual wavefront, and thus iterative wavefront correction is needed. It should be noted that, in our work, it is assumed that the DM can generate the aberration compensation amount very fast and can completely correct the aberration; meanwhile, the CCD camera can complete the image acquisition in high speed, and all the required matrix information has been calculated in advance. Thus, the time overhead is only cost on solving the drive voltage by the images. Although

iterative correction is required, each iteration is directly calculated by the analytical matrix, so the algorithm is quite fast.

## 4. SIMULATION RESULTS AND ANALYSIS

In our simulation experiment, the Kolmogorov model [18] is used to simulate the phase screens of the atmospheric turbulence. The phase is composed by 3rd–21st-order Zernike polynomials, and there is no correlation between different phase screens. The magnitude of turbulence strengths is indicated by  $D/r_0$ , where  $D$  represents the optical system caliber and  $r_0$  is for atmospheric coherence length. The larger the value of  $D/r_0$ , the worse the atmospheric conditions and the stronger the strengths of atmospheric turbulence. The relevant parameters of the optical system in the simulation experiment are as follows. The diameter of the optical system is  $2m$ , the  $F^\#$  of the system is 14, the size of the CCD pixel is  $8 \mu\text{m}$ , the sampling grid of the image plane is  $64 \times 64$ , and the number of sampling grids of the pupil plane is  $32 \times 32$  to satisfy the Nyquist sampling criterion. The noise of the CCD camera is 10 dB, and the defocus distance is set as 1 mm. The host control computer we used is Intel Core i7-4790K, and the frequency is 4.00 GHz. Different values of atmospheric coherence length are generated to simulate the atmospheric turbulence of different strengths. Here we choose three situations:  $r_0 = 10 \text{ cm}$ ,  $r_0 = 15 \text{ cm}$ , and  $r_0 = 20 \text{ cm}$ , respectively. Then, the corresponding values of  $D/r_0$  are 20, 13, and 10, respectively.

Figure 3 shows the wavefront variations under the three atmospheric turbulence strengths with respect to the number of correction steps during the calibration process. The detailed wavefront RMS variation values are given in Table 1. It can be seen that when  $D/r_0 = 20$ , the wavefront aberration was corrected from  $0.6764\lambda$  RMS to  $0.0098\lambda$  RMS by driving the DM seven times through the closed-loop algorithm. When  $D/r_0 = 13$ , after five adjustments of the DM, the wavefront aberration was corrected from  $0.4959\lambda$  RMS to  $0.0031\lambda$  RMS. When  $D/r_0 = 10$ , the wavefront aberration was corrected from  $0.3229\lambda$  RMS to  $0.0011\lambda$  RMS after only four times adjustment.

In order to test the effectiveness and validity of the closed-loop algorithm, under the three coherence lengths of atmosphere, we repeat 128 experiments for each situation to generate 384 sets of wavefront aberrations in total randomly. The statistical results are shown in Fig. 4, given in the form of error bars. The RMS of residual wavefront aberration after correction is used as an evaluation standard. The smaller residual error, the better the correction effect. For each error bar, the middle part represents the statistical mean value, the edge represents the maximum and minimum values after the outliers are discarded, and the value greater than or equal to twice the original mean value is defined as the outliers. In Fig. 4, the statistical results of the residual aberrations varying with the correction steps are given. When  $D/r_0 = 20$ , the mean value of residual aberration is approaching 0 after 6–7 times closed-loop correction; when  $D/r_0 = 13$ , most aberrations can be completely corrected after 4–5 iterations; when  $D/r_0 = 10$ , after 3–4 times of correction, the mean value of residual aberration is close to 0. The appearance of the outliers is due to the fact that the randomly generated wavefront aberrations are too large to be completely

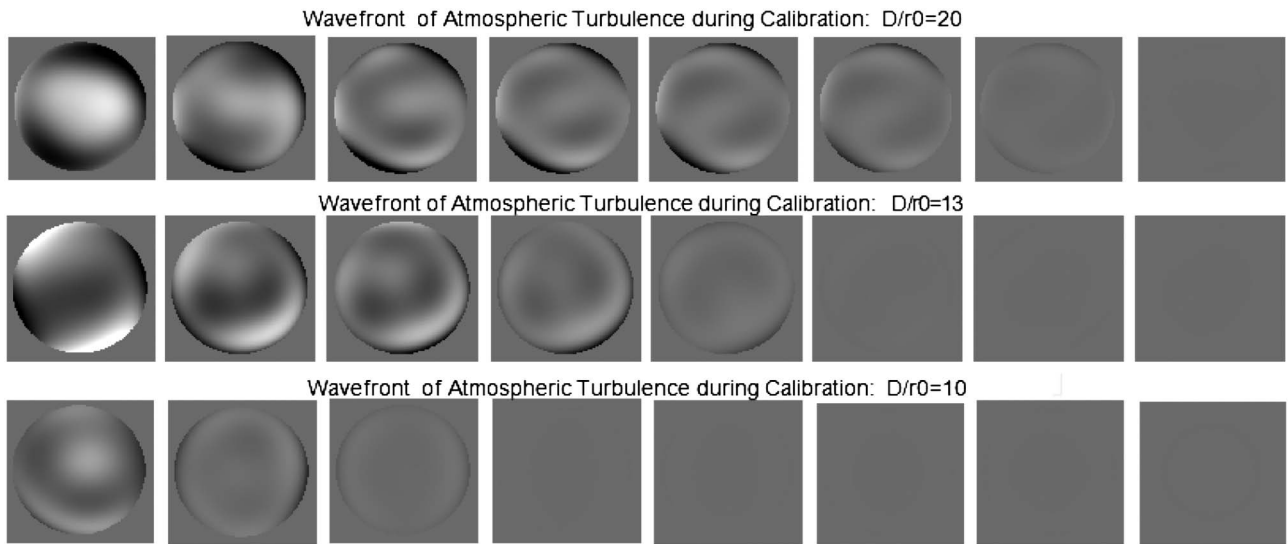


Fig. 3. Wavefront variations under the three atmospheric turbulence strengths with respect to the number of correction steps.

Table 1. Wavefront RMS Values ( $\lambda$ ) Varying with the Number of Correction Steps Under the Three Typical Atmospheric Coherence Lengths

$D/r_0$	Iterations							
	0	1	2	3	4	5	6	7
20	0.6764	0.4715	0.4067	0.3292	0.2302	0.1705	0.0637	0.0098
13	0.4959	0.3932	0.2856	0.1973	0.1016	0.0031	0.0008	0.0001
10	0.3229	0.2118	0.1128	0.0027	0.0011	0.0000	0.0000	0.0000

corrected in seven calibrations and need more iteration times. It can be seen from the figure that the wavefront correction range is quite wide, and after a few number of calibration steps, we can achieve a good wavefront correction effect.

In order to verify the convergence speed of the algorithm, the statistical results of the time required for complete correction of 384 sets of wavefront aberrations, 128 sets for each situation, are given in Fig. 5. The run time of the algorithm is obtained on the host control computer Intel Core i7-4790K,

4.0 GHZ. Figure 5(a) shows the time needed for completely correcting the wavefront aberrations for the three situations in the form of a scatter plot and Figs. 5(b)–5(d) give the histograms of the time consumed in each case. From Fig. 5(a), we can see that the cost time of all experiments is of the order of  $10^{-2}$  s and as the strength of atmospheric turbulence increases, the wavefront aberrations get larger, and the correction time is

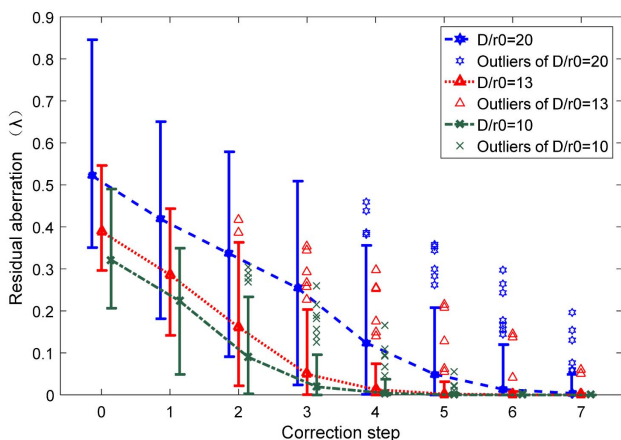


Fig. 4. Residual errors under three atmospheric turbulence strengths varying with the correction steps.

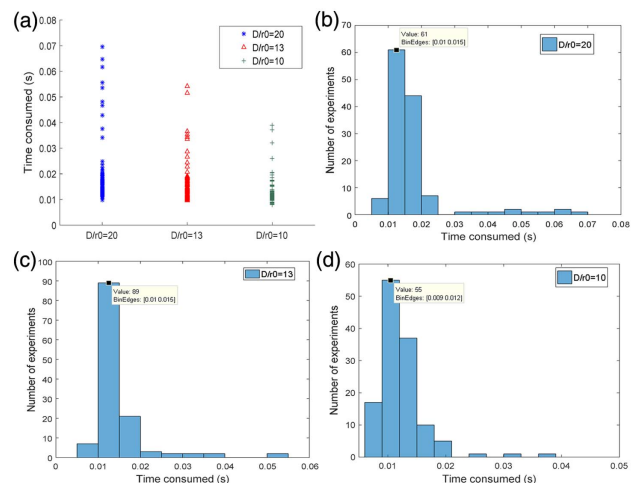


Fig. 5. Time consumed for complete correction of 384 (128  $\times$  3) sets of wavefront aberrations.

longer. Figure 5(b) shows that when  $D/r_0 = 20$ , 4.7% out of 128 simulations the wavefront correction time is 0.005–0.01 s; 82% out of 128 simulations the correction time is 0.01–0.02 s; the longest correction time is 0.07 s; and the statistical mean, median, and standard deviations of the correction time for these 128 simulations are 0.0179 s, 0.0149 s, and 0.0113 s, respectively. Figure 5(c) shows the results of  $D/r_0 = 13$ : 5.5% of 128 simulations the wavefront correction time is 0.005–0.01 s; 85.9% the correction time is 0.01–0.02 s; the longest correction time is 0.055 s; and their mean, median, and standard deviations of the correction time are 0.0147 s, 0.013 s, and 0.0069 s, respectively. While, in Fig. 5(d), 22.7% of 128 simulations the wavefront correction time is 0.005–0.01 s; 71.8% the correction time is 0.01–0.02 s; the longest correction time is 0.039s for  $D/r_0 = 10$ ; and the mean, median, and standard deviations of the correction time under this condition are 0.0125 s, 0.0115 s, and 0.0042 s, respectively. From the simulation results, we can see that the algorithm is quite fast. It should be noted that convergence speed of the algorithm is related to the size of the collected images; in our case, the size of the images is  $64 \times 64$  pixels. The smaller the size of the images, the faster the algorithm. Therefore, we can intercept the images to shrink the size to improve the algorithm speed, but the images must be registered. The specific registration method can refer to [19].

In order to verify the image quality of the system during the calibrations and illustrate the method’s correction capability in a more vivid way at the same time, a successive of six spot images collected in the focal plane from the first to sixth iterations are shown in Fig. 6 under the condition  $D/r_0 = 20$ . The Strehl ratio (SR) is adopted to evaluate the images, and the SR is defined as

$$SR = \frac{P[I(x, y)]}{P[I_0(x, y)]}, \tag{17}$$

where  $P[]$  is an operation that calculates the peak intensity,  $I$  is the actual intensity distribution, and  $I_0$  is the intensity distribution when no aberrations are present. The closer the SR value is approaching to 1, the better the spot quality is and the more ideal correction effect is gained. The SR values of the six images from Figs. 6(a)–6(f) are 0.0579, 0.2312, 0.4628, 0.7125, 0.8024, and 0.9302, respectively. It can be

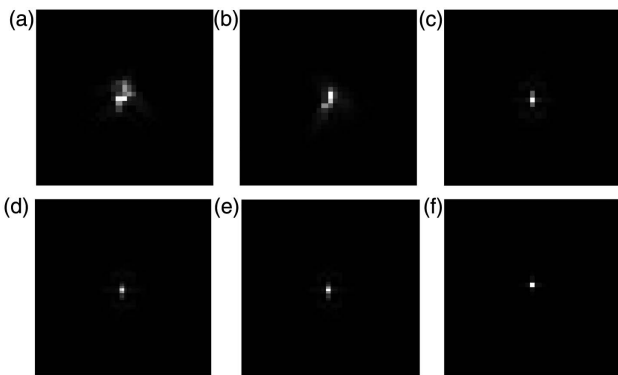


**Fig. 6.** Successive images collected in focal plane from the first to sixth iterations during wavefront aberration corrections when  $D/r_0 = 20$ .

seen from the results that during the calibration process, the spot energy becomes more and more concentrated. Thus, the system can continually correct wavefront aberrations and gain the ideal imaging results ultimately.

In order to test the performance of the presented method more fully, we compare our method with the model-based wavefront correction method proposed by Yang *et al.* [20] to observe unresolved point source under four different turbulence strengths, namely  $D/r_0 = 5, 10, 15, 20$ . For each turbulence strength, 128 frames of phase screens are generated randomly to test Yang’s and our method at the same time. The averaged RMS of the 128 sets of residual wavefronts are used to compare the correction capability of the two methods. The smaller the RMS value is, the better correction capability the method has. The averaged RMS of the two methods varying with the number of iterations is shown in Fig. 7. The icons “Method 1” and “Method 2” in the figure correspond to the method proposed by Yang *et al.* and our method, respectively.

From the averaged curves in Fig. 7, we can see that Yang’s method basically needs only one iteration to converge but the convergence accuracy is not as high as our proposed method. In fact, the convergence speed of Yang’s method only depends on the number of actuators of the DM and is independent of the turbulence strength, and the total measurements of the CCD data for one iteration is  $N + 1$ , where  $N$  is the number of actuators of the DM. It means that  $N + 1$  measurements of the CCD data are needed at least for Yang’s method. However, unlike Yang’s, our method only depends on the turbulence strength and for each iteration only one measurement of the CCD data is needed. It seems we need more iterations to get higher convergence accuracy, but in fact, the times of detector measurements are much less than Yang’s method. From the simulation results shown in Fig. 7, it needs 7–8 detector measurements on average to get higher convergence accuracy even for quite strong turbulence strength, while Yang needs 62 measurements since they use 61-element DM in [20]. Thus, our

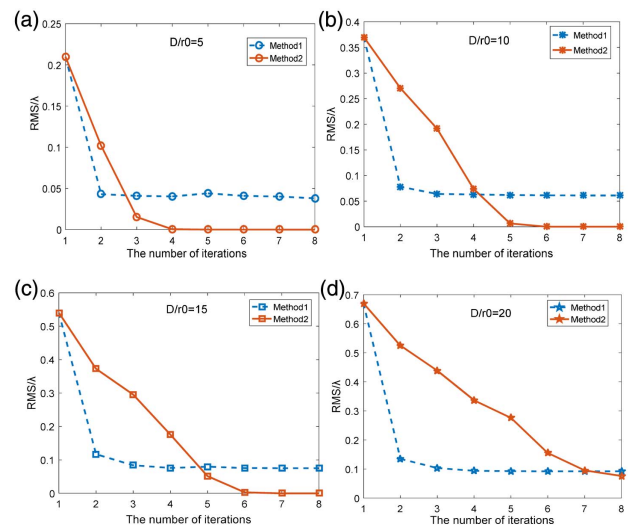


**Fig. 7.** Averaged RMS of the Yang’s (Method 1) and our methods (Method 2) varying with the number of iterations under four different turbulence strengths.

method needs fewer measurements of CCD data and gets higher convergence accuracy in the end.

## 5. CONCLUSION

In order to reach optimum results for the WFSless AO system, an efficient correction method is needed. A fast wavefront correction method for the WFSless AO system mainly based on the linear PD technique is presented in this paper. Combined with the influence function of the DM, we utilize the linear PD technique to establish the linear relationship model between the drive voltage of the DM and the far-field images of the system, and then the fast correction of wavefront aberrations is realized according to the established linear relationship model. Random wavefront aberrations are generated under different turbulence strengths and a large number of closed-loop correction simulations are carried out.

From the simulation results, it can be seen that the proposed method has a fast convergence rate and strong correction ability, a few correction times can fulfill good correction results, and can effectively improve the imaging quality of the system. It is also simple in implementation since the fast wavefront correction is realized only by using the far-field images. When comparing with the model-based wavefront correction method, the presented method has higher convergence accuracy and needs fewer measurements of CCD data.

**Funding.** National Natural Science Foundation of China (NSFC) (51505078).

## REFERENCES

1. R. K. Tyson, *Principles of Adaptive Optics* (Academic, 2010).
2. M. C. Roggemann and B. Welsh, "Adaptive optical imaging systems," in *Imaging through Turbulence* (CRC Press, 1996), pp. 182–183.
3. V. Lukin and B. Fortes, "Phase-correction of turbulent distortions of an optical wave propagating under conditions of strong intensity fluctuations," *Appl. Opt.* **41**, 5616–5624 (2002).
4. D. Débarre, E. J. Botcherby, T. Watanabe, S. Srinivas, M. J. Booth, and T. Wilson, "Image-based adaptive optics for two-photon microscopy," *Opt. Lett.* **34**, 2495–2497 (2009).
5. M. Jie, J. Feng, W. Xiao, Q. Zhu, Z. Li, and J. Zhang, "Error control of piston and tilt based on SPGD in coherent beam combination," *Chin. J. Lasers* **41**, 17–21 (2014).
6. H. Ma, Z. Liu, X. Xu, and J. Chen, "Simultaneous adaptive control of dual deformable mirrors for full-field beam shaping with the improved stochastic parallel gradient descent algorithm," *Opt. Lett.* **38**, 326–328 (2013).
7. S. Zommer, E. N. Ribak, S. G. Lipson, and J. Adler, "Simulated annealing in ocular adaptive optics," *Opt. Lett.* **31**, 939–941 (2006).
8. P. Yang, M. Ao, Y. Liu, B. Xu, and W. Jiang, "Intracavity transverse modes controlled by a genetic algorithm based on Zernike mode coefficients," *Opt. Express* **15**, 17051–17062 (2007).
9. Y. Liu, J. Ma, and B. Li, "Hill-climbing algorithm based on Zernike modes for wavefront sensorless adaptive optics," *Opt. Eng.* **52**, 016601 (2013).
10. A. Facomprez, E. Beaurepaire, and D. Débarre, "Accuracy of correction in modal sensorless adaptive optics," *Opt. Express* **20**, 2598–2612 (2012).
11. M. A. Neil, M. J. Booth, and T. Wilson, "Closed-loop aberration correction by use of a modal Zernike wave-front sensor," *Opt. Lett.* **25**, 1083–1085 (2000).
12. H. Song, R. Fraanje, G. Schitter, H. Kroese, G. Vdovin, and M. Verhaegen, "Model-based aberration correction in a closed-loop wavefront-sensor-less adaptive optics system," *Opt. Express* **18**, 24070–24084 (2010).
13. H. Linhai and C. Rao, "Wavefront sensorless adaptive optics: a general model-based approach," *Opt. Express* **19**, 371–379 (2011).
14. M. R. Bolcar and J. R. Fienup, "Sub-aperture piston phase diversity for segmented and multi-aperture systems," *Appl. Opt.* **48**, A5–A12 (2009).
15. D. Yue, S. Y. Xu, and H. T. Nie, "Co-phasing of the segmented mirror and image retrieval based on phase diversity using a modified algorithm," *Appl. Opt.* **54**, 7917–7924 (2015).
16. H. Z. Yang, B. Chen, X. Y. Li, and W. H. Jiang, "Experimental demonstration of stochastic parallel gradient descent control algorithm for adaptive optics system," *Acta Opt. Sinica* **28**, 205–210 (2008).
17. H. Z. Yang, W. Jian, and C. L. Gong, "Model-based sensorless adaptive optics system," *Acta Opt. Sinica* **34**, 7–11 (2014).
18. R. J. Noll, "Zernike polynomials and atmospheric turbulence," *J. Opt. Soc. Am. A* **66**, 207–211 (1976).
19. D. Yue, S. Y. Xu, H. T. Nie, and Z. Y. Wang, "An efficient correction algorithm for eliminating image misalignment effects on co-phasing measurement accuracy for segmented active optics systems," *Plos One* **11**, e0148872 (2016).
20. H. Z. Yang, O. Soloviev, and M. Verhaegen, "Model-based wavefront sensorless adaptive optics system for large aberrations and extended objects," *Opt. Express* **23**, 24587–24601 (2015).